# Low-Power, Low-Noise, FM MEMS Gyroscope: 3-Axis Sensor and Integrated Electronics Design

***Abstract*—This paper reports the developments towards an integrated, triaxial, frequency-modulated, consumer-grade, MEMS gyroscope. A custom low-power (160 µA), low-phase-noise integrated circuit is designed specifically for frequency-modulated operation. Both yaw- and pitch-rate sensing systems are demonstrated, by coupling the circuit with two novel micromachined structures fabricated with a 24-µm-thick industrial process. In operation, both gyroscopes show a repeatable and stable scale factor, with less than 0.55% of part-to-part variability, obtained without any calibration, and 35 ppm/° C of variability over a 25° to 70° C temperature range.**

***Index Terms*—Microelectromechanical devices, gyroscopes, frequency modulation.**

## I. Introduction

PRODUCING cheap and stable vibratory MEMS gyroscopes that do not require expensive and time-consuming calibration procedures has proven to be challenging, due to the dependence of the scale factor on fabrication imperfections and environmental changes [1].

Conventional microgyroscopes, operated as amplitude-modulated (AM) systems [2], [3], are sensitive to the accuracy of the drive mode displacement control [4], [5], to the value of the frequency mismatch between drive and sense modes [6], and to electronic gains in the sense readout chain. The result is a significant scale factor variability over both (i) offline unavoidable process spreads, and (ii) online variations of the ambient temperature ($T$) and humidity ($RH$). For manufacturers, a large amount of the cost of consumer-grade MEMS gyroscopes is thus given by expensive calibration routines: (i) the scale factor must be tuned on every sample at the rate table, and (ii) its dependence across the $T$-$RH$ operating range must be measured on a representative number of samples, to apply post-acquisition corrections. Resulting performance limitations, such as residual scale factor drifts due to imperfect calibration, generally preclude their widespread adoption in forthcoming applications, e.g., inertial grade navigation and pedestrian dead reckoning.

An alternative architecture for angular rate sensors is represented by MEMS gyroscopes where the rate information is frequency-modulated (FM) onto the resonance frequency of the micromachined structure [7]–[12], rather than amplitude-modulated onto the displacement along one of its mechanical modes. FM sensing benefits from a direct frequency output, the ease of interfacing with digital signal processing, and large dynamic range. Seshia *et al.* [7] first proposed a gyroscope where the Coriolis force modulates the stiffness of a resonant structure; in their configuration, however, the scale factor still depends on the drive displacement, as in AM gyroscopes.

In more recent FM implementations, the scale factor turns out to be a dimensionless quantity that depends only on the angular gain of the structure, thus significantly lowering the scale factor sensitivity to environmental variables and process spreads [10]. In addition to the advantages in reducing calibration time and costs, the FM approach promises benefits in the aforementioned applications where stability is of great concern. Zotov *et al.* [8] measured the rate from the observed split in the instantaneous frequency of the two primary modes of an ultra-high-Q structure, fabricated with a non-industrial process. Kline *et al.* [9] extracted the rate from the resonance frequency difference between two adjacent, matched resonators. Tsukamoto *et al.* [11] inferred the rate from the measured split between simultaneously-excited clockwise and counterclockwise modes on the same structure. All these methods share similar, power-hungry requirements for continuous frequency tracking needed for mode-matching.

One very promising FM approach was proposed by Izyumin *et al.* [12]. They realized a small-footprint FM gyroscope, by implementing continuous-time mode reversal, also referred to as Lissajous FM (LFM) operation. By letting a mechanical structure with two main orthogonal vibration modes oscillate at each mode's resonance, an angular rate oriented orthogonally to both modes is inferred from a resonance-frequency variation measurement. This working principle (i) uses a single proof mass, thus avoiding strict specifications on temperature mismatch otherwise required when using more than one structure; (ii) not only it requires no mode matching, but the split value has also no influence on the scale factor; (iii) by implementing continuous-time reversal, slow natural frequency drifts are not aliased as rate variations. Their published prototype is, however, implemented with discrete electronics, and only demonstrates yaw-rate sensing.

This work addresses the challenges of (i) developing a low-power integrated circuit (IC), and (ii) designing the structures of both yaw and pitch (or roll) sensing in an industrial process, thus giving perspectives on a full 3-axis FM system implementation.

Concerning point (i), in an LFM gyroscope, the required scale factor stability is obtained at the cost of a relatively small scale factor value, lower than 1 Hz / 360 dps. Targeting, e.g., a 10 mdps/$\sqrt{\text{Hz}}$ resolution, the needed frequency noise density is lower than 30 µHz/$\sqrt{\text{Hz}}$. This translates in an ultra-low-phase-noise requirement on the electronic circuitry, which should be, at the same time, low-power for always-on applications, making an integrated electronics design not trivial. FM gyroscopes presented in the literature only showed electronics either based on discrete components [8] or partially integrated, reaching at best a resolution of few tens of mdps/$\sqrt{\text{Hz}}$ [12].

Concerning point (ii), a challenge in the development of 3-

axis FM gyroscopes is the design of in-plane sensing systems, as one of the operational modes should move out of plane: due to the planarity of the micromachining process, this breaks the symmetry of the vibration pattern, increasing the complexity of both the mechanical design and the control electronics.

The paper is organized as follows. Section II describes the working principle of the developed FM gyroscopes and details the design of the two mechanical structures, for yaw and pitch (or roll) rate sensing; the structures are fabricated with STMicroelectronics thick-film epitaxial polysilicon surface-micromachining process [13], commonly used for mass production of MEMS inertial sensors. Section III describes the development of the integrated, low-noise, low-power oscillator, designed for FM operation, fabricated with a 0.35-µm CMOS process. Section IV reports experimental measurements on the tested samples demonstrating the feasibility of a sub-500-µA, ± 2000 dps full-scale, sub-10-mdps/$\sqrt{\text{Hz}}$ noise, 50-Hz bandwidth, 3-axis gyroscope, with 5500 ppm scale factor stability including part-to-part and temperature changes.

## II. Mechanical Design

### A. Working Principle

An LFM gyroscope relies on letting each orthogonal axis of a 2-DOF (degrees of freedom) mechanical structure, modeled as in Fig. 1a, oscillate at its own resonance frequency. An electronic circuit overcomes mechanical losses, and excites each resonator with a constant, controlled motion amplitude, equal for both axes. The natural frequencies of the two axes, $f_{nx}$ and $f_{ny}$, are, by design, different by an amount $f_\Delta$, so that the proof mass precesses in the *xy*-plane following the so-called Lissajous trajectory. In presence of an angular rate orthogonal to the plane of motion, the Coriolis force couples the two modes, inducing a resonance frequency variation measured at the sustaining electrodes. Since the center frequencies of the two oscillators are different, the angular rate information gets modulated at the frequency split given by $f_\Delta$, as graphically suggested by the force balance diagram of Fig. 1b. The reader can note how the Coriolis vector rotates in the phasor plane at a speed given by $f_\Delta$, thus periodically acting along the elastic force axis, thus determining the AM modulation of the FM signal. The rotation of the Coriolis vector indeed results in an equivalent sinusoidal modulation of the stiffness of the system, thus of the resonance frequency of each mode, whose expression as a function of the angular rate, $\Omega$, derived from the equation shown in Fig. 1b, is reported in Eq. (1):

$$f_{rx}(t) = f_{nx} - \alpha_{xy}\frac{v_{ya}}{v_{xa}}\Omega\sin(2\pi f_\Delta t), \qquad (1)$$

where $f_{nx}$ is the natural frequency of the considered mode, $v_{xa} = x_a 2\pi f_{rx}$ and $v_{ya} = y_a 2\pi f_{ry}$ are the velocity amplitudes of the motions of the considered mode and the orthogonal one, respectively, and $\alpha_{xy} \leq 1$ is the angular gain of the structure, a modal-mass-related coefficient that quantifies the Coriolis-induced coupling between the two modes. As an example, Fig. 1c graphically reports the time evolution of the resonance frequency of one axis in an ideal LFM gyroscope, with a 25-kHz natural frequency, 100-Hz mode split, unity angular gain, and perfect velocity amplitude control, as a function of a step-like angular rate, drawn as a dashed curve. Note that thanks to the AM modulation resonance frequency drifts, e.g., due to $T$-$RH$ variations or long-term aging, do not get modulated, and therefore are not aliased as rate signals, as they would be, e.g., in quadrature FM operation [9].

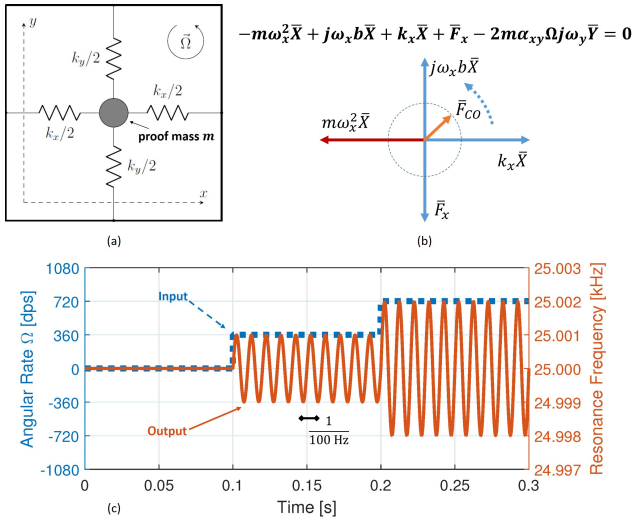


Fig. 1. Working principle of a LFM gyroscope. (a) A 2-DOF mechanical structure with two main vibration modes orthogonal one another; in presence of a rate directed orthogonally to both modes, the Coriolis force couples the two modes. (b) In a phasor diagram related to one resonant mode, the Coriolis force rotates at the mode-split frequency, $f_\Delta$. The resonance frequency can be found by nulling the net force alongside the x-axis (while y-axis relates with the amplitude of oscillation). (c) Example of the AM-modulation of the FM signal typical of LFM operation (with unity angular gain, velocity amplitude control, and 100-Hz mode split).

The angular rate is more conveniently inferred by measuring the sum of the instantaneous resonators frequencies:

$$f_\Sigma(t) = f_{nx} + f_{ny} - \alpha_{xy}\left(\frac{v_{ya}}{v_{xa}} + \frac{v_{xa}}{v_{ya}}\right)\Omega\sin(2\pi f_\Delta t). \qquad (2)$$

When summing the two channels, the signal-to-noise ratio increases. In addition, the scale factor depends on the product between the angular gain and the reciprocal sum of the velocity amplitude ratios. In this way, any amplitude-control-related error is minimized [12], and an ultra-stable, ratiometric scale factor is obtained, equal to twice the angular gain, i.e., $2\cdot\alpha_{xy}$.

In a more realistic model, Eq. (2) should include also aniso-stiffness and aniso-damping terms [14]. The complete expression becomes

$$\begin{aligned} f_\Sigma(t) \quad &= f_{nx} + f_{ny} - \alpha_{xy}\left(\frac{v_{ya}}{v_{xa}} + \frac{v_{xa}}{v_{ya}}\right)\Omega\sin(2\pi f_\Delta t) + \\ &+\alpha_{xy}\left(\frac{v_{ya}}{v_{xa}}I_x - \frac{v_{xa}}{v_{ya}}I_y\right)\sin(2\pi f_\Delta t) + \\ &+\alpha_{xy}\left(\frac{v_{ya}}{v_{xa}}Q_x + \frac{v_{xa}}{v_{ya}}Q_y\right)\cos(2\pi f_\Delta t). \qquad (3) \end{aligned}$$

where $I_{x,y}$, referred to as offset, comes from the aniso-damping term, while $Q_{x,y}$, referred to as quadrature, represents the effect of non-zero non-diagonal terms of the stiffness matrix. It is worth noting that, for symmetric aniso-damping terms, offset vanishes when summing the two frequencies.

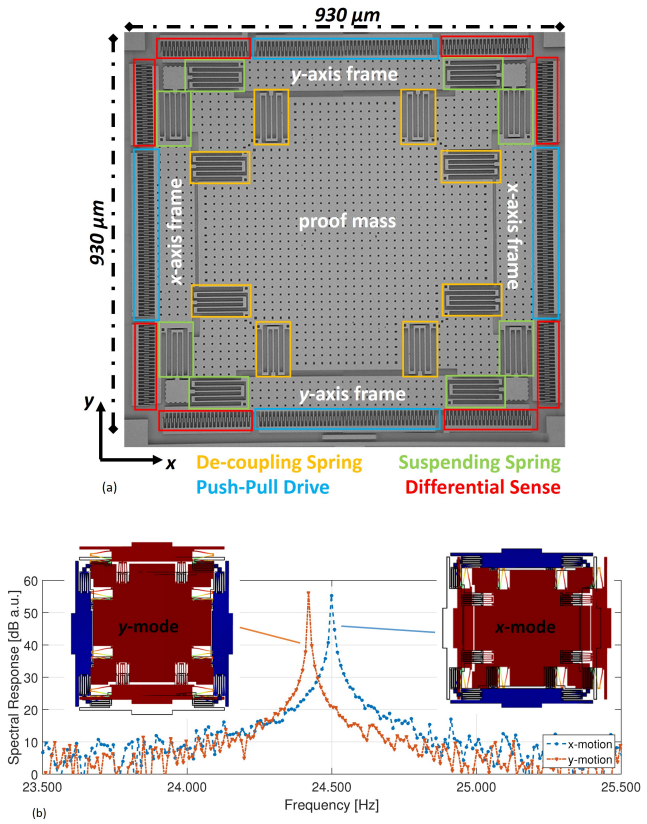


Fig. 2. (a) Optical microscope top-view of the 24-µm-thick yaw-rate-sensing gyroscope, and (b) corresponding first two mechanical modes with measured spectral responses.

### B. In-Plane Structure for Yaw-Rate Sensing

Figure 2a reports a micrograph of the mechanical structure developed for yaw-rate sensing. The structure, adapted to the used industrial process from the design described in [15], is formed by four external frames, suspended through 2 folded springs each, and by a proof mass, nested inside the frames and decoupled through 8 further springs. Push-pull actuation and fully-differential sensing are provided through 1.8-µm comb fingers designed on the external frames. The ratio between the modal mass coupled through the Coriolis force and the overall modal mass contributes to set the angular gain, whose expected value is 0.8.

The two resonators are designed with a nominal 100-Hz mode split, enabling a yaw-rate sensing system with a 50-Hz bandwidth. To this purpose, a 0.8% mass difference is set, by design, between the two resonators. The nominal resonance frequencies are set around 25 kHz, as a good trade-off between acoustic and vibration rejection, and electronics power consumption minimization. Actual mode split values may change from sample to sample, due to process over-/under-etch. This spread has no macroscopic effect on scale factor, linearity, or full-scale. On the other hand, a maximum sensing bandwidth reduction is required if the mode split gets reduced, to avoid aliasing effects, while resolution linearly worsens with the mismatch.

Since the structure is free of parallel plates, as no tuning of the mode split is required, the sensitivity being independent of this parameter, both resonators show high quality factors, with measured values around 15 000, at a nominal bonding pressure of 0.7 mbar (see Fig. 2b).

The target displacement amplitude is set to 4 µm, limited to avoid any mechanical non-linearity that would worsen the resolution of the sensor, as will be shown in Section IV. The number of motion-detection fingers is maximized within the available area, giving a capacitance variation $C_a$ nominally equal to 40 fF per port; the motional current flowing out of the sense port is thus maximized, so to minimize phase noise.

### C. Out-of-Plane Structure for Pitch-Rate Sensing

Figure 3a reports a micrograph of the mechanical structure developed for pitch-rate sensing. The structure is formed by four external frames with the proof mass decoupled and nested in between. The two frames to generate in-plane motion are suspended through symmetric folded springs, with push-pull actuation and fully-differential sensing provided through comb fingers. The two frames for out-of-plane motion are suspended through torsional bars. Push-pull actuation and differential sensing are this time provided through parallel-plate electrodes designed underneath the frames as indicated in the figure. Four folded levers couple the frames to the proof mass, transforming the two torsional displacements into a vertical translation of the proof mass. According to the motion generated by the described frames, the proof mass, further decoupled from the in-plane frames through two levers having folds at each tip, orbits following a Lissajous trajectory along a plane orthogonal to the substrate. The expected value of the angular gain is 0.8, so to match the scale factor of the yaw sensor.

Due to the presence of parallel-plate electrodes, the out-of-plane resonator shows a lower quality factor, with measured values around 1100 (see Fig. 3b) at the given bonding pressure, compared to the 10 000 value of the comb-driven mode.

Some design strategies were adopted for such a pitch device, as its operating modes have inherently and widely different modal shapes, as well as different actuation and detection topologies. First, due to the constraints in the vertical gap, the design targets a maximum displacement of the proof mass along both directions of about 1 µm (≈ 4 times smaller than for the yaw sensor). Such an amplitude coincides with the displacement of the external frames for the in-plane motion, and corresponds to a maximum displacement of about 150 nm at the frames for out-of-plane motion, to limit driving and sensing electrostatic non-linearity for a vertical gap value of 1.8 µm. Additionally, the values of the driving and sensing capacitances are designed in such a way that the product of the capacitance variation per unit displacement at each resonator sensing port, multiplied by the electrode effective motion, is similar (around 40 fF) for the two modes, so to provide the same output current at both resonators output ports, and thus the same phase noise for the two oscillators of the pitch gyroscope. As the mentioned capacitance variations are also close to the ones of the yaw sensor, both yaw and pitch gyroscopes can be operated with the same electronic circuitry.

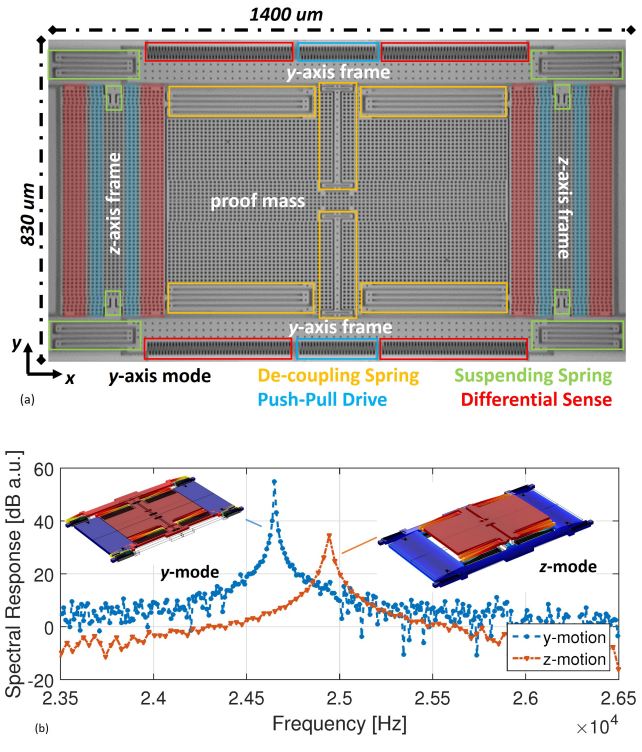


Fig. 3. (a) Optical microscope top-view of the 24-µm-thick pitch-rate-sensing gyroscope, and (b) corresponding first two mechanical modes with measured spectral responses.

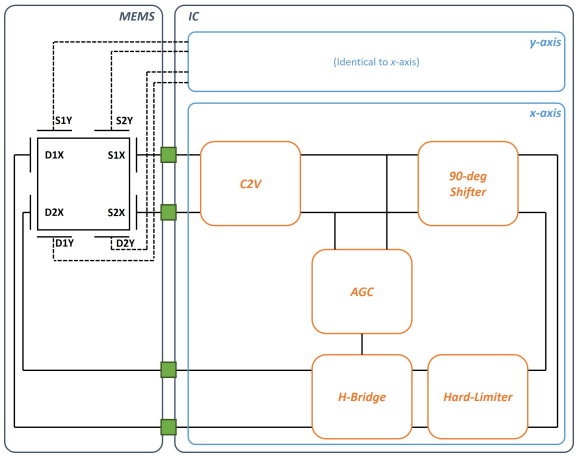


Fig. 4. Schematic of the system, showing the MEMS on the left and the IC on the right, with an insight of one of the two oscillators.

## III. Electronics Design

As anticipated in Section II, the electronic circuitry required for FM operation basically consists of two oscillators, to keep each mode in stable oscillation at resonance. In addition, each circuit should provide an oscillation-amplitude control loop, required to keep stable the scale factor shown in Eq. (2). These requirements are matched while minimizing the power consumption, so to have an ultra-low-power sensor.

### A. Circuit Topology and Architectural Choices

There are two different approaches that well fit the high-Q property of the MEMS resonators of the proposed FM gyroscope: feedback oscillators [16], and Pierce oscillators [17]. Pierce oscillators are simple circuits with few transistors and capacitors, and very low power consumption. However, Pierce oscillators do not provide means of implementing motion amplitude control. The feedback oscillator architecture was thus chosen for this work. A MEMS feedback oscillator basically consists of a front-end, commonly referred to as capacitance-to-voltage amplifier (C2V), that senses the MEMS motion through a variation of the sense capacitance, and translates this signal into a voltage, which is then delivered to the resonator through the driving circuitry.

Figure 4 shows a schematic of the whole system. The two oscillators, identically replicated, are integrated in the same chip, fabricated with a 0.35-µm process. The IC core occupies an active area lower than 2 mm$^2$, integrated in a 4.5 mm$^2$ die.

Each oscillator, implemented with fully-differential stages to maximize the signal-to-noise ratio and supply-noise rejection, has roots on the topologies described in [18]. It consists of the C2V, a 90-deg shifter, required to satisfy Barkhausen criteria at resonance, a hard-limiter (HL), which implements the non-linear stage required for oscillation build-up and enables square-wave, hence low-power, driving, and an H-bridge, which delivers the drive actuation waveforms; its supply is provided by an automatic gain control (AGC) circuit. A detailed schematic of each oscillator is shown in Fig. 5, where the signals propagating around the loop are also shown.

The C2V is implemented as a charge amplifier. The implemented feedback network is composed of a 800-fF capacitor, whose value was chosen as a good compromise between maximizing the gain and minimizing the output distortion, and a pseudo-resistor, implemented with two back-to-back cross-coupled diode-connected PMOS transistors [19]; the equivalent resistance is larger than 10 GΩ, allowing a closed loop pole frequency lower than 20 Hz, far below the operating one. Note that a trans-resistance amplifier (TRA) needs an 8-MΩ resistor to obtain the same gain. This is incompatible with the noise requirements that call for a minimum resistance of 850 MΩ. The implemented operational transconductance amplifier (OTA), together with the common-mode feedback network, is reported in Fig. 6. The OTA1 relies on a single-stage, folded-cascode, fully-differential topology, with PMOS input pair to minimize flicker noise, and an overall consumption of 19 µA.

The 90-deg shifter, required to compensate the 90-deg shift introduced by the C2V, is distinctively implemented as an active integrator whose pole is far below 25 kHz. By suitably sizing the input resistor (1 MΩ) and the feedback capacitor (6.5 pF), around the operating frequency the stage behaves as a unity-gain, 90-deg phase shifter. The used OTA2 is similar to the one adopted for the C2V, with a smaller current consumption as its noise contribution is less relevant. The same pseudo-resistors used for C2V are implemented to bias the feedback network. An additional capacitor of 70 pF is added in series with the input resistor, so to introduce a DC de-coupling from the previous stage, thus rejecting any C2V offset.

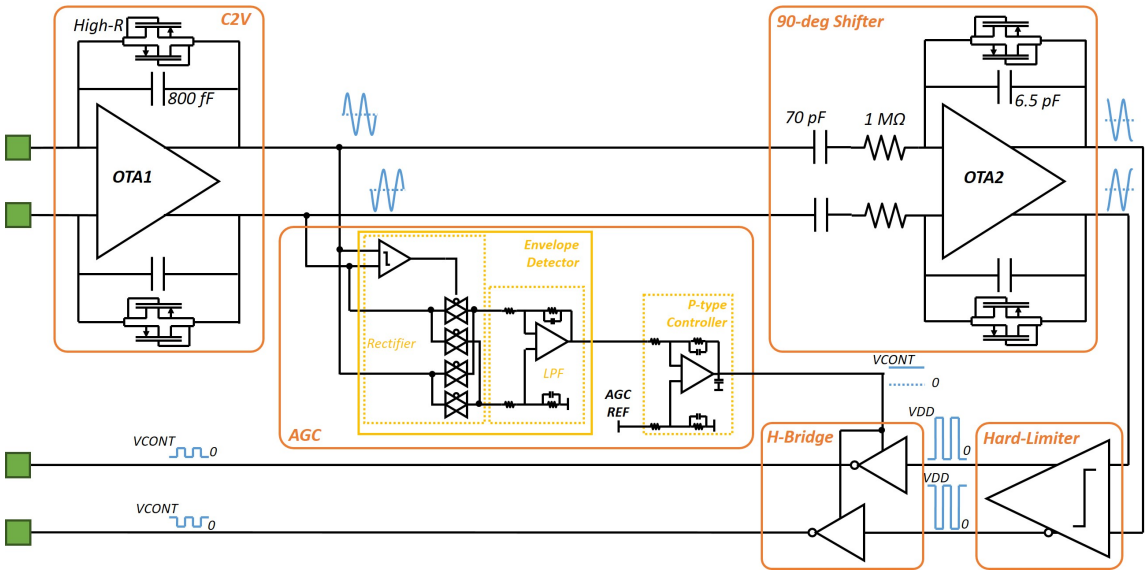


Fig. 5. Detailed schematic of the implemented oscillator, showing the AGC driving the H-Bridge supply (VCONT).

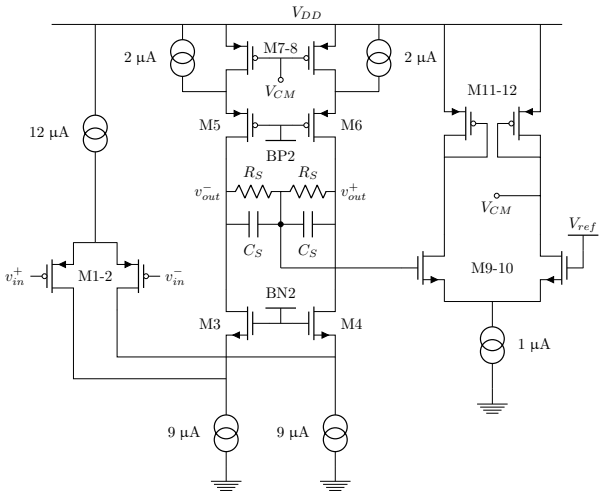


Fig. 6. Transistor-level schematic of C2V's OTA1, with its common-mode feedback network.

The hard-limiter is implemented with an open-loop OTA, while the H-bridge configuration was chosen as the amplitude controlling block, where the AGC output (VCONT in Fig. 5) simply sets the supply of the H-bridge itself. Both choices are motivated by low-power requirements. Indeed, such an implementation, based only on digital blocks, eliminates the need for power-hungry variable gain amplifiers.

The AGC is implemented as a negative-feedback loop that extracts motion amplitude information from the envelope of the waveform at the C2V output, compares it with a motion amplitude reference, and correspondingly adjusts the amplitude of the drive waveform. The envelope detector is implemented with a self-clocked passive mixer, which, combined with the subsequent low-pass filter, behaves as a standard AM-demodulator. The subsequent stage is the proportional-type controller of the AGC, implemented as a difference amplifier. One of its inputs is a DC voltage that equivalently fixes the target displacement amplitude. The gain of the stage is set to 50, and a low-pass filter is added, so to reduce the effects of second-harmonic tones coming from the mixer.

Note that with the chosen oscillator topology there is no node within the loop whose voltage is proportional to the velocity of the proof mass. In order to control the velocity amplitude, as required in Eq. (2), an additional differentiator stage should be implemented, thus increasing the overall power consumption of the system. However, starting from Eq. (2), one can derive the expression of the sum of the resonance frequencies when controlling the displacement amplitude, $x_a = y_a = x_{a,ref}$, rather than the velocity amplitude:

$$f_\Sigma(t) \simeq f_{nx} + f_{ny} - \alpha_{xy}\left(\frac{f_{ny}}{f_{nx}} + \frac{f_{nx}}{f_{ny}}\right)\Omega \sin(2\pi f_\Delta t)\,. \quad (4)$$

At such small mismatch value as the one chosen for the designed gyroscopes, a scale factor deviation of 8 ppm only with respect to constant-velocity conditions is experienced.

As shown in Fig. 7a, a large portion of current consumption is dedicated to the C2V, as its OTA thermal noise is the dominant noise source within the circuit. The current consumption of the AGC is high, as well, to allow its output stage to correctly drive its constantly-switching load, i.e., the H-bridge. The overall current consumption per oscillator is 80 µA.

### B. Resolution

As the signal of interest is a frequency variation, the minimum detectable rate (i.e., the resolution of the sensor) is strictly related to the phase (frequency) noise of the oscillator. To be more precise, as the rate information is frequency-modulated by the Lissajous pattern at the frequency of the mode split, as shown in Eq. (2), phase noise has itself to be evaluated and minimized at an offset $f_\Delta$ from the carrier.

Using conventional phase noise analysis in MEMS oscillators [20], the sensor turns out to be limited by electronics- rather than termo-mechanical-noise, for all the Q values of the

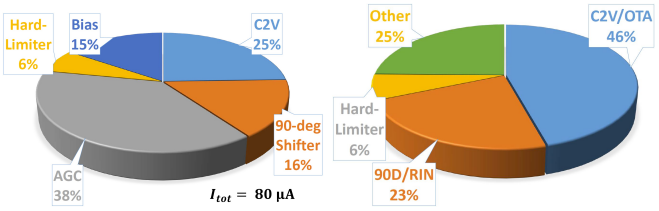


(a) (b)

Fig. 7. (a) Current consumption partitioning. At a DC supply of 3.3 V, the total power consumption is 0.26 mW only per oscillator. (b) Noise contribution partitioning: C2V/OTA refers to the thermal noise of OTA1; 90D/RIN refers to input resistors of the 90-deg shifter; HL refers to the input pair of the hard-limiting stage.

considered resonators. In particular, phase noise is limited by the additive noise introduced by the first stages of the electronic loop, whose power spectral density can be conveniently input-referred as an equivalent rate density:

$$S_{n\Omega} \simeq \frac{(360°)^2}{\alpha_{xy}^2} f^2 S_{n\phi}(f) = \frac{(360°)^2}{\alpha_{xy}^2} f^2 \frac{S_{nC,e}(f_{nx}+f)}{C_a^2}, \tag{5}$$

where $S_{n\Omega}$ is the input-referred rate noise expressed in dps$^2$/Hz, $S_{n\phi}$ is phase noise associated with the oscillation signal, $f$ is the frequency offset from the natural frequency, and $S_{nC,e}$ is the electronic noise, input-referred as equivalent capacitance noise. Two dominant noise sources were identified. The first one is the input pair of the OTA1 employed in the C2V, whose effects are amplified by the parasitic capacitor from the sense detection node to ground; to this purpose, custom-designed IC input pads were implemented, as in [19]. The second one is the thermal noise associated with the input resistor of the 90-deg shifter. Its noise contribution could have been easily lowered by simply reducing its value down to few hundreds of kiloohms. Such a relatively-low resistor would have affected, however, the stability performance of the C2V, and a consequent increase of its power consumption would have thus been necessary. The final 1-MΩ value was chosen as an optimal trade-off between noise, phase lag, and power consumption minimization. A pie chart of the different noise contributors is reported in Fig. 7b.

### C. Noise Folding Analysis

Particular attention was given to limit noise folding effects [21]–[23]. An active integrator topology was preferred to a phase-locked loop (PLL) to implement the 90-deg shifter. The integrator behaves, indeed, as an anti-aliasing filter in front of the hard-limiter, narrowing the bandwidth before folding occurs. As the noise bandwidth of the C2V is nominally 100 times larger than the oscillation frequency, its output is a sinusoidal voltage with wideband noise. If a hard-limiter is then directly connected to the C2V, it detects phase changes only at the zero crossings, i.e., only twice within an input signal period. Wideband noise of the C2V is under-sampled, and folded into the signal band, eventually worsening the sensor resolution. To overcome this issue, the solution of inserting an anti-noise-folding band-pass filter between the

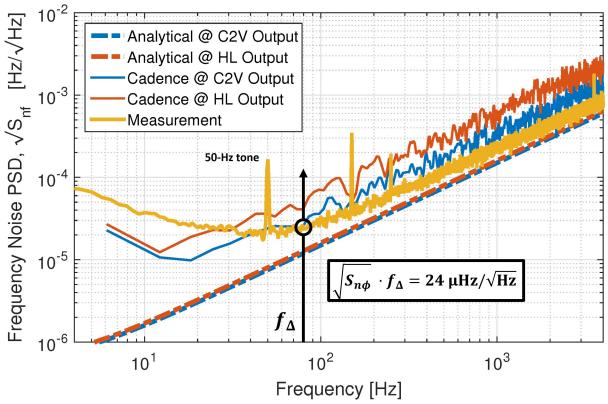


Fig. 8. Frequency noise spectra predicted at C2V and HL outputs. Thanks to the low-pass (anti-alias) implementation of the 90-deg shifter, worsening by noise folding is minimized. The measured frequency noise spectrum is shown for comparison.

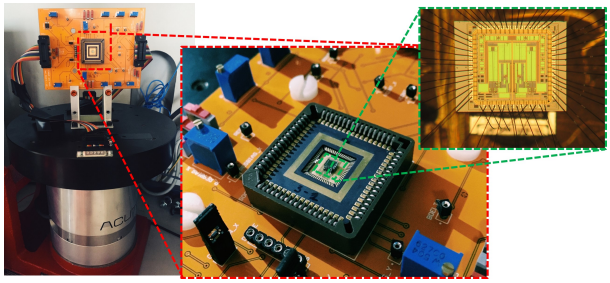

Fig. 9. For experimental measurements, the MEMS and the IC are stacked and wire-bonded in a socket, and then placed on the rate table.

C2V and the HL was adopted, employing the described 90-deg shifter.

Note that, if a conventional PLL with a standard input phase-frequency detector (PFD) was connected at C2V output, and used for the aforementioned 90-deg phase shift requirement [18], the PLL would operate like a sampled system in the phase domain, exactly as the hard-limiter, and noise folding would have drastically degraded the resolution of the sensor.

With the implemented circuitry, Fig. 8 shows the predicted spectra of frequency noise, $S_{nf}(f) = f^2 S_{n\phi}(f)$, of a single oscillator. A theoretical value of 13 µHz/√Hz at 80 Hz offset is predicted at the hard-limiter output, assuming a 5 pF parasitic capacitor at each input node. This translates into an estimated 6 mdps/√Hz gyro resolution. Thanks to the integrator-based shifter, the folding penalty is of 1.2 dB only, while it would have been of at least 14 dB using a PLL-based oscillator. Theoretical predictions were substantially confirmed with cadence© transient noise simulations, whose results are reported in Fig. 8 as well.

## IV. Experimental Measurements

Figure 9 shows the experimental setup. Each MEMS is wire-bonded to its own IC in a socket that is then installed onto the rate table.

For scale factor measurements, the oscillation frequency variation of each oscillator is measured using a bench-top frequency meter (Keysight 53230A), as a function of the

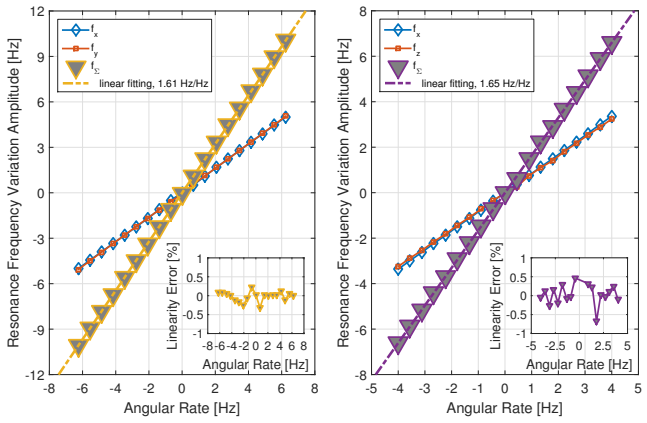


(a) Yaw (b) Pitch

Fig. 10. Scale factor measurements for yaw (a) and pitch (b) gyroscopes over $\pm$ 2250 dsp and $\pm$ 1140 dsp rates, respectively. The insets show the linearity error.

applied rate. The variations of the two axes are then summed up, to obtain the signal expressed in Eq. (3). The scale factor is obtained with a fitting model on measured data. For the sake of simplicity, half of the scale factor will be reported, as

$$\frac{S_\Sigma}{2} = \frac{S_x + S_y}{2} = \frac{1}{2}\alpha_{xy}\left(\frac{f_{ny}}{f_{nx}} + \frac{f_{nx}}{f_{ny}}\right), \qquad (6)$$

so that it can be compared more easily with the ones obtained from single-resonator measurements, $S_x$ and $S_y$, respectively. 8 yaw devices and 3 pitch devices, correspondingly coupled to 11 integrated circuits, were tested in order to verify experimentally the part-to-part repeatability of the scale factor.

Figure 10 reports a sample measurement for one yaw and one pitch sensing system. The obtained values of about 0.8 Hz/Hz are aligned with the predicted angular gain given in Section II. For both devices, as shown in the corresponding insets, a linearity error smaller than 0.6% of the maximum applied rate is extrapolated.

### A. Yaw Scale Factor Repeatability

Measured scale factors, $S_\Sigma/2$, of different yaw samples are reported in Fig. 11 by triangular markers. The figure describes the scale factor variability reduction obtained when considering the sum of the individual resonance frequency variations, shown with square and circular markers. The extrapolated relative standard deviation of the total scale factor is 5500 ppm, compared with a 3% spread when considering each axis on its own. It is worth noting that these results are obtained with neither setup nor post-processing calibrations, and even with a 280% variation between the lowest (67 Hz) and the largest (187 Hz) encountered mismatch values.

Scale factors on one sample performed at different temperatures are reported in Fig. 12. When fitting the data with a linear model, the extrapolated temperature coefficient of the scale factor (TCS) turns out to be $-35$ ppm/K, that corresponds to a 0.4% total variation within the whole consumer-grade range between $-40°$ and 80° C. Note that, even without any compensation/calibration procedure, this value is lower than

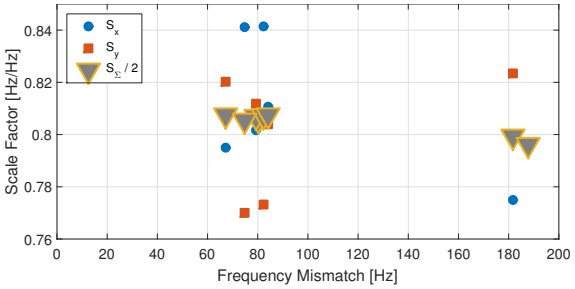


Fig. 11. Report on scale factor measurements performed on eight different yaw samples, as a function of the obtained frequency mismatch.

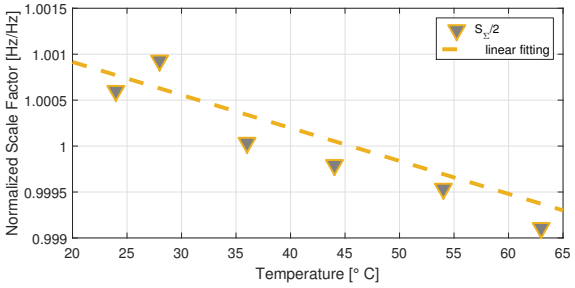


Fig. 12. Report on scale factor measurements on a yaw sensor performed at different operating temperatures.

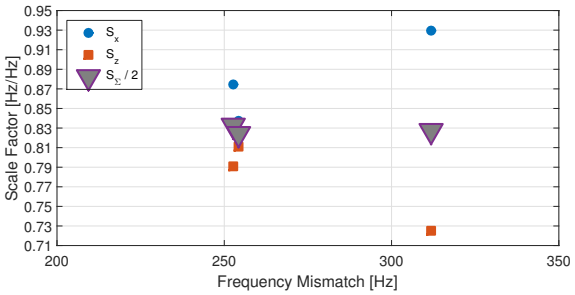


Fig. 13. Report on scale factor measurements performed on three different pitch samples, as a function of the obtained frequency mismatch.

the one reported in the datasheet of state-of-the-art commercial gyroscopes, whose performance are summarized in Table I.

Measured average quadratures, $Q_x$ and $Q_y$ terms of Eq. (3), for the tested yaw samples are 450 dps.

### B. Pitch Scale Factor Repeatability

Scale factors of three different pitch samples are reported in Fig. 13 by triangular markers. The extrapolated relative standard deviation of the total scale factor, $S_\Sigma$, is 5400 ppm, comparable with the one obtained for the yaw gyroscope.

Measured average quadrature for the tested pitch samples is 4000 dps, likely dominated by skew angle issues [27].

### C. Noise

Figure 8 shows a frequency noise measurement performed on one yaw sample, compared with theoretical predictions. As shown in Eq. (5), in order to infer the noise equivalent rate density, one should evaluate the noise PSD at the frequency mismatch, $S_{nf}(f = f_\Delta)$, i.e., 80 Hz for the considered

TABLE I
PERFORMANCE COMPARISON BETWEEN THE PROPOSED GYROSCOPE AND STATE-OF-THE-ART COMMERCIAL PRODUCTS

| **Manufacturer** | **Device** | **Scale factor change** | **Temperature range** [° C] | **Current consumption** (gyro only) [mA] |
|---|---|---|---|---|
| | This work | −0.0035%/K (over temperature)<br>±0.55% (part-to-part) | 20 to 70 | 0.6 |
| STMicroelectronics | 6D IMU LSM6DSL [24] | ±0.007%/K (over temperature)<br>±1% (part-to-part) | −40 to 85 | 0.6 |
| Invensense | 6D IMU ICM-20600 [25] | ±2% (over temperature)<br>±1% (part-to-part) | −40 to 85 | 2.5 |
| Bosch Sensortec | 6D IMU BMI160 [26] | ±0.02%/K<br>±3% (part-to-part) | −40 to 85 | 0.9 |

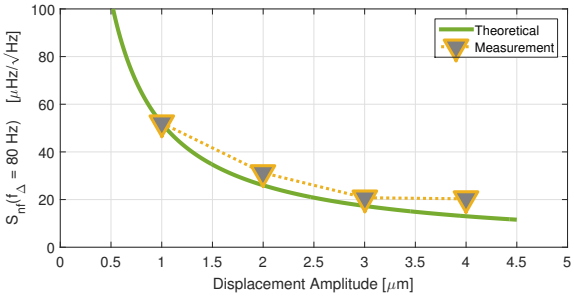


Fig. 14. Frequency noise PSD evaluated at 80-Hz offset as a function of the displacement amplitude of the proof mass of a yaw gyroscope.

sample, and divide it by the scale factor. The measured value of 24 μHz/$\sqrt{\text{Hz}}$ (Fig. 8) translates into a 10.8 mdps/$\sqrt{\text{Hz}}$ noise equivalent rate density. Note that the variability in the frequency mismatch, which, as shown, did not impact on the scale factor, reflects instead on the resolution, that ranges from 9 to 24 mdps/$\sqrt{\text{Hz}}$ when considering all the tested samples.

Figure 14 shows the dependence of the frequency noise of the same yaw sample on the displacement amplitude of the proof mass, obtained by changing the AGC reference. The figure shows how the noise density is inversely proportional to the displacement amplitude, as predicted by Eq. (5). The deviation between experimental data and predictions is likely due to an underestimation of the parasitic capacitors at the input nodes of the C2V. The flattening of the measured noise at displacements larger than 3 μm might be ascribed to mechanical non-linearities of the springs at large displacements.

Noise on the pitch gyroscope is on average 5 times larger than the minimum noise measured for the yaw sensor, in line with the larger mismatch obtained for the fabricated pitch devices. A partial re-design of this sensor is needed to match a smaller split and hence to reach comparable noise performance at the same offset frequency.

## V. CONCLUSION

This work demonstrates a low-power, low-phase-noise integrated circuit for frequency-modulated sensors, applied to the case of yaw and pitch/roll Lissajous FM gyroscopes. The main achieved result is the demonstration of 0.5% scale factor repeatability and 35 ppm/K stability over temperature, at 160 μA current consumption only, while holding noise performance around 10 mdps/$\sqrt{\text{Hz}}$. The shown system can be combined with a frequency digitization circuit [28], to deliver a sub-6-mm$^2$, 600 μA overall consumption, fully-integrated, digital-output, 3-axis MEMS gyroscope, providing at the same time lower consumption and better scale factor stability than state-of-the-art sensors.

Theoretical analyses and system-level considerations for the design of a monolithic 3-axis LFM gyroscope and its related electronics to deliver even lower consumption performance (375 μA) are currently ongoing.

## REFERENCES


[1] C. Acar and A. Shkel, *MEMS Vibratory Gyroscopes: Structural Approaches to Improve Robustness*, 2nd ed. Springer Publishing Company, Incorporated, 2008.

[2] N. Yazdi, F. Ayazi, and K. Najafi, "Micromachined inertial sensors," *Proc. IEEE*, vol. 86, DOI 10.1109/5.704269, no. 8, pp. 1640–1659, Aug. 1998.

[3] R. N. DeanJr. and A. Luque, "Applications of microelectromechanical systems in industrial processes and services," *IEEE Transactions on Industrial Electronics*, vol. 56, DOI 10.1109/TIE.2009.2013691, no. 4, pp. 913–925, Apr. 2009.

[4] I. P. Prikhodko, S. A. Zotov, A. A. Trusov, and A. M. Shkel, "Sub-degree-per-hour silicon MEMS rate sensor with 1 million Q-factor," in *2011 16th International Solid-State Sensors, Actuators and Microsystems Conference*, DOI 10.1109/TRANSDUCERS.2011.5969216, pp. 2809–2812, Jun. 2011.

[5] L. Dong and D. Avanesian, "Drive-Mode Control for Vibrational MEMS Gyroscopes," *IEEE Transactions on Industrial Electronics*, vol. 56, DOI 10.1109/TIE.2008.2010088, no. 4, pp. 956–963, Apr. 2009.

[6] G. Langfelder, S. Dellea, A. Berthelot, P. Rey, A. Tocchio, and A. F. Longoni, "Analysis of Mode-Split Operation in MEMS Based on Piezoresistive Nanogauges," *Journal of Microelectromechanical Systems*, vol. 24, DOI 10.1109/JMEMS.2014.2324032, no. 1, pp. 174–181, Feb. 2015.

[7] A. A. Seshia, R. T. Howe, and S. Montague, "An integrated microelectromechanical resonant output gyroscope," in *Technical Digest. MEMS 2002 IEEE International Conference. Fifteenth IEEE International Conference on Micro Electro Mechanical Systems*, DOI 10.1109/MEMSYS.2002.984372, pp. 722–726, Jan. 2002.

[8] S. A. Zotov, A. A. Trusov, and A. M. Shkel, "High-Range Angular Rate Sensor Based on Mechanical Frequency Modulation," *Journal of Microelectromechanical Systems*, vol. 21, DOI 10.1109/JMEMS.2011.2178116, no. 2, pp. 398–405, Apr. 2012.

[9] M. H. Kline, Y. C. Yeh, B. Eminoglu, H. Najar, M. Daneman, D. A. Horsley, and B. E. Boser, "Quadrature FM gyroscope," in *2013 IEEE 26th International Conference on Micro Electro Mechanical Systems (MEMS)*, DOI 10.1109/MEMSYS.2013.6474314, pp. 604–608, Jan. 2013.

[10] B. Eminoglu, Y. C. Yeh, I. I. Izyumin, I. Nacita, M. Wireman, A. Reinelt, and B. E. Boser, "Comparison of long-term stability of AM versus FM gyroscopes," in *2016 IEEE 29th International Conference on Micro Electro Mechanical Systems (MEMS)*, DOI 10.1109/MEMSYS.2016.7421790, pp. 954–957, Jan. 2016.

[11] T. Tsukamoto and S. Tanaka, "Fully-differential single resonator FM/whole angle gyroscope using CW/CCW mode separator," in *2017 IEEE 30th International Conference on Micro Electro Mechanical Systems (MEMS)*, DOI 10.1109/MEMSYS.2017.7863610, pp. 1118–1121, Jan. 2017.

[12] I. I. Izyumin, M. H. Kline, Y. C. Yeh, B. Eminoglu, C. H. Ahn, V. A. Hong, Y. Yang, E. J. Ng, T. W. Kenny, and B. E. Boser, "A 7ppm, 6 deg/hr frequency-output MEMS gyroscope," in *2015 28th IEEE International Conference on Micro Electro Mechanical Systems (MEMS)*, DOI 10.1109/MEMSYS.2015.7050879, pp. 33–36, Jan. 2015.

[13] G. Langfelder, C. Buffa, A. Frangi, A. Tocchio, E. Lasalandra, and A. Longoni, "Z-Axis Magnetometers for MEMS Inertial Measurement Units Using an Industrial Process," *IEEE Transactions on Industrial Electronics*, vol. 60, DOI 10.1109/TIE.2012.2210958, no. 9, pp. 3983–3990, Sep. 2013.

[14] M. Kline, "Frequency Modulated Gyroscopes," Ph.D. dissertation, EECS Department, University of California, Berkeley, May. 2015. [Online]. Available: http://www2.eecs.berkeley.edu/Pubs/TechRpts/2015/EECS-2015-26.html

[15] I. Izyumin, B. E. Boser, and M. H. Kline, "Frequency readout gyroscope," Jun. 2014, WO Patent App. PCT/US2013/074,835. [Online]. Available: https://www.google.com/patents/WO2014093727A1?cl=en

[16] C. T. C. Nguyen and R. T. Howe, "An integrated CMOS micromechanical resonator high-Q oscillator," *IEEE Journal of Solid-State Circuits*, vol. 34, DOI 10.1109/4.753677, no. 4, pp. 440–455, Apr. 1999.

[17] E. A. Vittoz, M. G. R. Degrauwe, and S. Bitz, "High-performance crystal oscillator circuits: theory and application," *IEEE Journal of Solid-State Circuits*, vol. 23, DOI 10.1109/4.318, no. 3, pp. 774–783, Jun. 1988.

[18] L. Aaltonen and K. A. I. Halonen, "An analog drive loop for a capacitive MEMS gyroscope," *Analog Integrated Circuits and Signal Processing*, vol. 63, DOI 10.1007/s10470-009-9395-6, no. 3, pp. 465–476, 2010.

[19] P. Minotti, S. Brenna, G. Laghi, A. G. Bonfanti, G. Langfelder, and A. L. Lacaita, "A Sub-400-nT/$\sqrt{}$Hz, 775-$\mu$W, Multi-Loop MEMS Magnetometer With Integrated Readout Electronics," *Journal of Microelectromechanical Systems*, vol. 24, DOI 10.1109/JMEMS.2015.2452316, no. 6, pp. 1938–1950, Dec. 2015.

[20] P. Ward and A. Duwel, "Oscillator phase noise: systematic construction of an analytical model encompassing nonlinearity," *IEEE Trans. Ultrason., Ferroelectr., Freq. Control*, vol. 58, DOI 10.1109/TUFFC.2011.1786, no. 1, pp. 195–205, Jan. 2011.

[21] C. Samori, A. L. Lacaita, F. Villa, and F. Zappa, "Spectrum folding and phase noise in LC tuned oscillators," *IEEE Transactions on Circuits and Systems II: Analog and Digital Signal Processing*, vol. 45, DOI 10.1109/82.700925, no. 7, pp. 781–790, Jul. 1998.

[22] L. Aaltonen, M. Saukoski, I. Teikari, and K. Halonen, "Noise analysis of comparator performed sine-to-square conversion," in *Electronics Conference, 2006 International Baltic*, DOI 10.1109/BEC.2006.311071, pp. 1–4, Oct. 2006.

[23] J. Zhao, X. Wang, Y. Zhao, G. M. Xia, A. P. Qiu, Y. Su, and Y. P. Xu, "A 0.23-$\mu$g Bias Instability and 1-$\mu$g/$\sqrt{}$Hz Acceleration Noise Density Silicon Oscillating Accelerometer With Embedded Frequency-to-Digital Converter in PLL," *IEEE Journal of Solid-State Circuits*, vol. 52, DOI 10.1109/JSSC.2016.2645613, no. 4, pp. 1053–1065, Apr. 2017.

[24] *LSM6DSL: iNEMO inertial module, always-on 3D accelerometer and 3D gyroscope*, STMicroelectronics, 2016.

[25] *ICM-20600: High Performance 6-Axis MEMS MotionTracking Device*, InvenSense Inc., 2016.

[26] *BMI160: small, low power inertial measurement unit*, Bosch Sensortec, 2015.

[27] M. S. Weinberg and A. Kourepenis, "Error sources in in-plane silicon tuning-fork MEMS gyroscopes," *Journal of Microelectromechanical Systems*, vol. 15, DOI 10.1109/JMEMS.2006.876779, no. 3, pp. 479–491, Jun. 2006.

[28] I. Izyumin, M. Kline, Y. C. Yeh, B. Eminoglu, and B. Boser, "A 50 $\mu$W, 2.1 mdeg/s/$\sqrt{}$Hz frequency-to-digital converter for frequency-output MEMS gyroscopes," in *ESSCIRC 2014 - 40th European Solid State Circuits Conference (ESSCIRC)*, DOI 10.1109/ESSCIRC.2014.6942106, pp. 399–402, Sep. 2014.